Bayesian Image Reconstruction in Quantitative Photoacoustic Tomography

Tanja Tarvainen*, Aki Pulkkinen, Ben T. Cox, Jari P. Kaipio, and Simon R. Arridge

***Abstract*—Quantitative photoacoustic tomography is an emerging imaging technique aimed at estimating chromophore concentrations inside tissues from photoacoustic images, which are formed by combining optical information and ultrasonic propagation. This is a hybrid imaging problem in which the solution of one inverse problem acts as the data for another ill-posed inverse problem. In the optical reconstruction of quantitative photoacoustic tomography, the data is obtained as a solution of an acoustic inverse initial value problem. Thus, both the data and the noise are affected by the method applied to solve the acoustic inverse problem. In this paper, the noise of optical data is modelled as Gaussian distributed with mean and covariance approximated by solving several acoustic inverse initial value problems using acoustic noise samples as data. Furthermore, Bayesian approximation error modelling is applied to compensate for the modelling errors in the optical data caused by the acoustic solver. The results show that modelling of the noise statistics and the approximation errors can improve the optical reconstructions.**

***Index Terms*—Bayesian methods, biomedical optical imaging, inverse problems, photoacoustic effects, tomography, ultrasonic imaging.**

I. Introduction

PHOTOACOUSTIC tomography (PAT) is an emerging imaging modality developed over the last few decades which combines the benefits of optical contrast and ultrasound propagation. The optical methods provide information about the distribution of chromophores which are light absorbing molecules within the tissue. The chromophores of interest are, for example, haemoglobin, melanin, and various contrast agents. The ultrasonic waves carry this optical information directly to the surface with minimal scattering, thus retaining accurate spatial information as well. Nowadays, PAT can be used to provide images of soft biological tissues with high spatial resolution. It has successfully been applied to the visualization of different structures in biological tissues such as human blood vessels, microvasculature of tumors and cerebral cortex in small animals. However, this information is only a qualitative image and it does not include quantitative information about chromophores' concentrations. For more information about PAT, see e.g., [1]–[4], and the references therein.

Quantitative photoacoustic tomography (QPAT) is a technique in which also the absolute concentration of chromophores is estimated [5]. This is a hybrid imaging problem in which the solution of one inverse problem acts as a data for another ill-posed inverse problem. The two inverse problems in QPAT are: 1) reconstruct the initial acoustic pressure distribution from measured acoustic waves and 2) reconstruct the distributions of the optical parameters from the absorbed optical energy density.

The first inverse problem 1) is an inverse initial value problem in acoustics. There are a large number of reconstruction techniques available, see e.g., [1], [3], [6] and the references therein. However, in cases in which the speed of sound, acoustic absorption and scattering within the tissue are varying, the inverse problem becomes significantly more challenging [7]–[16].

The second inverse problem in QPAT 2) is the optical image reconstruction. In the optical inverse problem the goal is to estimate the concentrations of chromophores. These can be obtained either by directly estimating the distributions of concentrations from photoacoustic images obtained at various wavelengths or by first recovering the absorption coefficients at different wavelengths and then calculating the concentrations from the absorption spectra [5]. In order to obtain accurate estimates, scattering effects also need to be taken into account [5], [17]–[19]. In this work, estimation of absorption and scattering at one wavelength is considered. Extension to multiple wavelengths is straightforward. For more information about multiwavelength PAT, see e.g., [5], [20]–[25], and the references therein.

Different approaches for the solution of the optical inverse problem have been considered, see e.g., [17]–[20], [22], [23], [26]–[40]. In this work, we consider the optical inverse problem of QPAT in a Bayesian framework [41], [42]. In the Bayesian approach for inverse ill-posed problems, all parameters are

Manuscript received June 19, 2013; revised July 24, 2013; accepted August 27, 2013. Date of publication August 30, 2013; date of current version November 25, 2013. This work was supported in part by the Academy of Finland (projects 136220, 140984, and 250215 Finnish Centre of Excellence in Inverse Problems Research), in part by the Engineering and Physical Sciences Research Council (EPRSC), and in part by the strategic funding of the University of Eastern Finland. *Asterisk indicates corresponding author.*

*T. Tarvainen is with the Department of Applied Physics, University of Eastern Finland, 70211 Kuopio, Finland, and also with the Department of Computer Science, University College London, WC1E 6BT London, U.K. (e-mail: tanja.tarvainen@uef.fi).

A. Pulkkinen is with the Department of Applied Physics, University of Eastern Finland, 70211 Kuopio, Finland (e-mail: aki.pulkkinen@uef.fi).

B. T. Cox is with the Department of Medical Physics and Bioengineering, University College London, WC1E 6BT London, U.K. (e-mail: b.cox@ucl.ac.uk).

J. P. Kaipio is with Department of Mathematics, University of Auckland, Auckland 1142, New Zealand, and also with the Department of Applied Physics, University of Eastern Finland, 70211 Kuopio, Finland (e-mail: jari@math.auckland.ac.nz).

S. R. Arridge is with the Department of Computer Science, University College London, WC1E 6BT London, U.K. (e-mail: s.arridge@cs.ucl.ac.uk).

Color versions of one or more of the figures in this paper are available online at http://ieeexplore.ieee.org.

Digital Object Identifier 10.1109/TMI.2013.2280281

modelled as random variables. The parameters depend on each other through a model and information about the parameters is expressed by probability distributions. In the inverse problem, the idea is to estimate the unknown parameters based on the measurements, the model and the prior information about the parameters.

In tomographic inverse problems, measurement noise is generally modelled as uncorrelated Gaussian distributed with zero mean and known (constant) variance. In the optical inverse problem of QPAT, the data is obtained as a solution of the acoustic inverse initial value problem. Thus, the data and noise are affected by the method applied to solve the acoustic inverse problem. Therefore, the noise of the optical data has a different distribution from the noise of the acoustic measurement. Furthermore, the optical data contains modelling errors caused by the acoustic solver.

In this paper, the Bayesian approach is used in the modelling of the noise statistics of the optical data and its application to the solution of the optical inverse problem. Furthermore, approximation error modelling is considered. The Bayesian approximation error approach for the treatment of modelling errors was introduced in [41], [43]. The method has previously been successfully applied in other ill-posed tomographic imaging problems for example in compensating modelling errors due to discretization, domain mismodelling and model reduction [44]–[53]. In this paper, the approximation error method is applied to compensate for the errors in the optical data caused by the acoustic solver.

The rest of the paper is organized as follows. Quantitative photoacoustic tomography and the related forward and inverse problems are described in Section II. The Bayesian approach for the optical inverse problem, and the modelling of noise and approximation errors, are described in Section III. The results of simulations are shown in Section IV and the conclusions are given in Section V.

II. Quantitative Photoacoustic Tomography

In QPAT, a short (ns) pulse of near-infrared light is used to illuminate the region of tissue of interest. As light propagates within the tissue, it is absorbed by chromophores. This generates localized increases in pressure. This pressure increase propagates through the tissue as an acoustic wave and is detected by ultrasound sensors on the surface of the tissue. The propagation of the acoustic wave occurs on a microsecond time scale, about five orders of magnitude slower than the optical propagation, so only the total absorbed optical energy density is of interest and not the rate of the absorption. This large difference in the time scale allows the optical and acoustic parts of the inverse problem to be decoupled and treated separately.

A. Forward Problem

The forward problem in QPAT is to solve the time-varying pressure on the boundary of the target when the optical and acoustic properties and the amount of input light are given. Solving the QPAT forward problem consist of solving optical and acoustic forward problems.

1) Optical Forward Problem: Let $r \in \mathbb{R}^d$ be a point located in a tissue region of interest $\Omega \subset \mathbb{R}^d$ with boundary $\partial\Omega$ where $d = 2, 3$ is the dimension of the domain. The optical forward problem in QPAT is to compute the absorbed optical energy density when the optical properties of the medium and the input light sources are given. In this work, we use the diffusion approximation (DA) to the radiative transfer equation as the model for light propagation [54]. The DA together with a Robin-type boundary condition is of the form

$$-\nabla \cdot \kappa(r)\nabla\Phi(r) + \mu_a(r)\Phi(r) = 0 \quad r \in \Omega \tag{1}$$

$$\Phi(r) + \frac{1}{2\gamma_d}\kappa(r)\frac{\partial\Phi(r)}{\partial\hat{n}} = \begin{cases} \frac{I_s}{\gamma_d}, & r \in \epsilon_j \\ 0, & r \in \partial\Omega \setminus \epsilon_j \end{cases} \tag{2}$$

where $\Phi(r)$ is the fluence, $\mu_a(r)$ is the absorption coefficient, $\kappa(r) = (d(\mu_a(r) + \mu_s'(r)))^{-1}$ is the diffusion coefficient and $\mu_s'(r) = (1-g)\mu_s(r)$ is the reduced scattering coefficient, where $\mu_s(r)$ is the scattering coefficient and g is the mean of the cosine of the scattering angle [41], [54]. Further, I_s is a diffuse boundary current at the source position $\epsilon_j \subset \partial\Omega$, γ_d is a dimension-dependent constant which takes values $\gamma_2 = 1/\pi$ and $\gamma_3 = 1/4$ and $\hat{n}$ is an outward unit normal [41]. The absorbed optical energy density $H(r)$ can be solved from fluence as

$$H(r) = \mu_a(r)\Phi(r). \tag{3}$$

In this work, a finite element method (FEM) is used for the numerical solution of the DA [18].

The absorbed energy density is connected to the initial acoustic pressure distribution $p_0(r)$ through the photoacoustic efficiency which can be identified with the Grüneisen parameter for an absorbing fluid [5]. In this work, the Grüneisen coefficient is assumed to be a known constant G and the initial acoustic pressure distribution is

$$p_0(r) = p(r, t=0) = GH(r). \tag{4}$$

2) Acoustic Forward Problem: The acoustic forward problem in QPAT is to solve the time-varying pressure $p(r,t)$ at the detectors surrounding the object. Time evolution of the photoacoustic wave fields can be modelled using the equations of linear acoustics [55]. For soft biological tissues, it is generally assumed that the medium is isotropic and quiescent and that the shear waves can be neglected. The propagation of pressure through an acoustically nonabsorbing medium is described by wave equation [56]

$$\nabla^2 p(r,t) - \frac{1}{c^2}\frac{\partial^2 p(r,t)}{\partial t^2} = 0 \tag{5}$$

where c is the speed of sound which in this work is assumed to be a known constant. The wave equation (5) is solved together with initial conditions (4) and

$$\frac{\partial p(r, t=0)}{\partial t} = 0. \tag{6}$$

A perfectly matched layer (PML) is applied at the boundaries to simulate free space propagation. In this work, the numerical solution of the wave equation is obtained using the k-space time-domain method implemented with the k-Wave MATLAB toolbox [55].

B. Inverse Problem

The inverse problem in QPAT is to solve the distribution of optical parameters in the medium when the measured pressure on the detectors and the amount of input light are given. Generally, the acoustic properties of the medium and the Grüneisen coefficient are assumed to be known. However, correction of artefacts due to unknown acoustic parameters have also been considered [7], [9], [11], [13], [14], [16], [57]. Furthermore, simultaneous estimation of the optical parameters and the Grüneisen coefficient have been investigated [17], [23], [34], [38].

1) Acoustic Inverse Problem: The first inverse problem in QPAT is the acoustic inverse initial value problem in which the initial acoustic pressure distribution $p_0(r)$ is estimated when measured acoustic waves p_S on the detectors are given. In this work, we use a time reversal method from the k-Wave MATLAB toolbox for the solution of the acoustic inverse problem [55]. In this approach, the recorded measurements $p_S(t)$ are used in time-reversed order as a time-varying Dirichlet boundary condition at the detector positions. The time evolution of the propagating acoustic wave field imposed by the Dirichlet boundary condition is calculated using the wave equation (5) with zero initial conditions. The reconstructed initial pressure p_0 is then obtained as an acoustic pressure within the domain after time T. In this work, the medium is assumed to be nonabsorbing and the speed of sound is assumed to be known.

2) Optical Inverse Problem: The second inverse problem in QPAT is to estimate the optical parameters when the absorbed optical energy density and the input illumination are given. In this work we use the Bayesian approach for the solution of the optical inverse problem and estimate the absorption and scattering distributions within the domain. The approach is described in Section III.

III. Bayesian Approach for the Optical Inverse Problem of QPAT

Let us denote the distribution of optical parameters at a point r by $x(r) := (\mu_a(r), \mu_s(r))^{\mathrm{T}}$. Further, denote the measurements by a finite dimensional vector $y = (H_1, \ldots, H_m)^{\mathrm{T}} \in \mathbb{R}^m$ where m is the number of measurements which in this case is the number of illuminations multiplied with the number of discretized elements to represent the data space. The observation model with an additive noise model is of the form

$$y = A\left(x(r)\right) + e \tag{7}$$

where A is the forward model which maps the parameters to the measurable data, and e denotes the noise. Typically in practical implementations the parameters and the forward mapping are represented in discrete vector spaces $x(r) \mapsto x \in \mathbb{R}^N, A \mapsto A_h : \mathbb{R}^N \to \mathbb{R}^m$ and the continuous model (7) is replaced by an approximate equation

$$y = A_h(x) + e \tag{8}$$

where x is a discretized parameter distribution and A_h is a discretized forward model.

In the Bayesian approach, the inverse problem is treated as a problem of statistical inference [41], [42]. All variables are modelled as random variables and the measurements are used to determine the posterior probability density of the parameters of primary interest.

Let us assume that x and y are random variables in finite-dimensional spaces $\mathbb{R}^N$ and $\mathbb{R}^m$ called parameter and data space, respectively. The joint probability density of x and y can be written in terms of conditional probability densities as

$$\pi(x, y) = \pi(x)\pi(y|x) = \pi(y)\pi(x|y). \tag{9}$$

The solution of the inverse problem is the posterior probability density $\pi(x|y)$ which according to (9) is of the form

$$\pi(x|y) = \frac{\pi(x)\pi(y|x)}{\pi(y)} \tag{10}$$

where $\pi(x)$ is the prior probability density and $\pi(y|x)$ is the likelihood density [41], [42]. Equation (10) is the Bayes' formula, and it is typically written in the nonnormalized form

$$\pi(x|y) \propto \pi(y|x)\pi(x) \tag{11}$$

since $\pi(y)$ is constant for fixed measurements y. If we assume that the noise e and the unknown x are mutually independent, formula (8) leads to likelihood density

$$\pi(y|x) = \pi_e\left(y - A_h(x)\right) \tag{12}$$

where π_e is the probability distribution of the noise e.

If the unknown x and the measurement errors can be modelled as Gaussian random variables, we have

$$x \sim \mathcal{N}(x_*, \Gamma_x), \quad e \sim \mathcal{N}(e_*, \Gamma_e)$$

where $x_* \in \mathbb{R}^N$ and $e_* \in \mathbb{R}^m$ are the means and $\Gamma_x \in \mathbb{R}^{N\times N}$ and $\Gamma_e \in \mathbb{R}^{m\times m}$ are the covariance matrices. In this case, the posterior density (11) becomes

$$\pi(x|y) \propto \exp\left\{-\frac{1}{2}\left(y - A_h(x) - e_*\right)^{\mathrm{T}}\Gamma_e^{-1}\left(y - A_h(x) - e_*\right) - \frac{1}{2}(x - x_*)^{\mathrm{T}}\Gamma_x^{-1}(x - x_*)\right\}. \tag{13}$$

A. Modelling of Noise

1) Conventional Noise Model: Typically in tomographic inverse problems, the mean of the noise is assumed to be zero, $e_* = 0 \in \mathbb{R}^m$, and the covariance is assumed to be a diagonal matrix with known (constant) variance σ, that is $\Gamma_e = \Gamma_\sigma = \mathrm{diag}(\sigma^2) \in \mathbb{R}^{\mathrm{m}\times\mathrm{m}}$. In this case, the posterior density (11) becomes

$$\pi(x|y) \propto \exp\left\{-\frac{1}{2\sigma^2}\left(y - A_h(x)\right)^{\mathrm{T}}\left(y - A_h(x)\right) - \frac{1}{2}(x - x_*)^{\mathrm{T}}\Gamma_x^{-1}(x - x_*)\right\}. \tag{14}$$

The practical solution for the inverse problem is obtained by calculating point estimates from the posterior density. Since we are interested in computationally efficient inverse problem solvers,

we consider here only the maximum *a posteriori* (MAP) estimate. It is obtained as

$$x_{\mathrm{MAP}} = \arg\max_x \{\pi(x|y)\} = \arg\min_x \left\{ \left\| \frac{1}{\sigma}\left(y - A_h(x)\right) \right\|^2 + \|L_x(x - x_*)\|^2 \right\} \quad (15)$$

where Cholesky factorization of the prior is $\Gamma_x^{-1} = L_x^{\mathrm{T}} L_x$. In the following sections, we refer to the solution of (15) as the MAP estimate with the conventional noise model (MAP-CNM). Generally, the optical inverse problem is solved using the conventional noise model by minimizing (15). In this case, the mean of the noise is set as zero and some value σ, which is thought to be most suitable, is chosen as the variance of the noise.

2) Approximate Noise Model: In practice, the noise is hardly ever uncorrelated and it has a nonzero mean, and thus the MAP estimate of posterior distribution (13) is obtained as

$$x_{\mathrm{MAP}} = \arg\min_x \left\{ \|L_e\left(y - A_h(x) - e_*\right)\|^2 + \|L_x(x - x_*)\|^2 \right\} \quad (16)$$

where Cholesky factorization of the noise is $\Gamma_e^{-1} = L_e^{\mathrm{T}} L_e$. In the following sections, we refer to the solution of (16) as the MAP estimate with an approximate noise model (MAP-ANM).

A more accurate noise model can be, for example, approximated as follows. First a set of noise samples of pressure measurements are simulated (or measured using an empty acoustic measurement setup). Then, the inverse initial value problem is solved using these noise samples as data. As a result, noise samples of the optical inverse problem $e^{(l)}$ are obtained. The mean and the covariance of the noise model can then be approximated using these noise samples as

$$e_* = \frac{1}{L}\sum_{l=1}^{L} e^{(l)} \quad (17)$$

$$\Gamma_e = \frac{1}{L-1}\sum_{l=1}^{L} e^{(l)} e^{(l)\mathrm{T}} - e_* e_*^{\mathrm{T}} \quad (18)$$

where L is the number of samples. These are then applied in the solution of the minimization problem (16).

B. Approximation Error Approach

In practice the numerical implementation of the acoustic inverse method also affects the measured data. Thus, the optical energy density distribution obtained as the solution of the acoustic inverse problem contains modelling error ε which can be due to e.g., discretization of the geometry and time, implementation of the boundary conditions and smoothing of the data by the acoustic solver.

Let us assume that the continuous model $x(r) \mapsto A(x(r))$, (7), can be approximated by a densely discretized finite-dimensional model

$$A_\delta : \mathbb{R}^N \to \mathbb{R}^m, \quad x \mapsto A_\delta(x), \quad \delta > 0 \text{ small}.$$

Thus, the discretized model, that is exact within the measurement accuracy, is of the form

$$y = A_\delta(x) + e. \quad (19)$$

In the approximation error approach [41], [43], the observation model is written in the form

$$y = A_h(x) + \left(A_\delta(x) - A_h(x)\right) + e = A_h(x) + \varepsilon(x) + e \quad (20)$$

where $A_h(x)$ is the reduced model and $\varepsilon(x)$ is the modelling error. The modelling error describes the discrepancy between the accurate forward model and the reduced model, i.e., a model that is an approximation to the accurate physical model and/or a model with a coarser discretization or a smaller computational domain [41], [43].

In the approximation error approach, a Gaussian approximation is constructed for ε, and the total error $n = \varepsilon + e$ is approximated by a Gaussian distribution, thus

$$\varepsilon \sim \mathcal{N}(\varepsilon_*, \Gamma_\varepsilon), \quad n \sim \mathcal{N}(n_*, \Gamma_n).$$

Furthermore, if we ignore the mutual dependence of x and ε, we get an approximation that is referred to as the enhanced error model [41]

$$\pi(x|y) \propto \exp\left\{ -\frac{1}{2}\left(y - A_h(x) - n_*\right)^{\mathrm{T}} \Gamma_n^{-1}\left(y - A_h(x) - n_*\right) - \frac{1}{2}(x - x_*)^{\mathrm{T}} \Gamma_x^{-1}(x - x_*) \right\} \quad (21)$$

where $n_* = \varepsilon_* + e_*$ and $\Gamma_n = \Gamma_\varepsilon + \Gamma_e$. The MAP estimate with the enhanced error model is obtained as [45]

$$x_{\mathrm{MAP}} = \arg\min_x \left\{ \|L_n\left(y - A_h(x) - n_*\right)\|^2 + \|L_x(x - x_*)\|^2 \right\} \quad (22)$$

where $\Gamma_n^{-1} = L_n^{\mathrm{T}} L_n$. In the following, we refer to the solution of (22) as the MAP estimate with the approximation error model approach (MAP-AEM). As it can be see, functional resembles penalized weighted least squares approach [58]–[61]. In addition, other work on related problems can be found in [62]–[64]. However, in the Bayesian approach taken here, the issue is how to compute the mean and the covariance of the noise and modelling errors.

The modelling error can be simulated for example as follows. First, a set of samples $\{x^{(\ell)}, \ell = 1, \ldots, M\}$ are drawn from the prior distribution $\pi(x)$ of the optical parameters. Then, the optical forward problem is solved in a fine discretization using these samples. This results a set of forward solutions $A_\delta(x^{(\ell)})$. Then, in order to obtain samples of the reduced forward model solutions, the acoustic forward and inverse problems of QPAT are solved. The obtained reconstructed initial pressure samples are used to calculate $A_h(x^{(\ell)})$. Then samples of the approximation error are computed as

$$\varepsilon^\ell = A_\delta\left(x^{(\ell)}\right) - A_h\left(x^{(\ell)}\right) \quad (23)$$

and the mean and covariance of the approximation error are estimated as

$$\varepsilon_* = \frac{1}{M}\sum_{\ell=1}^{M} \varepsilon^{(\ell)} \tag{24}$$

$$\Gamma_\varepsilon = \frac{1}{M-1}\sum_{\ell=1}^{M} \varepsilon^{(\ell)}\varepsilon^{(\ell)\mathrm{T}} - \varepsilon_*\varepsilon_*^{\mathrm{T}}. \tag{25}$$

These are then applied in the solution of the minimization problem (22) together with the noise model e.

We note that the mean and covariance of the noise model (17) and (18) and the approximation error model (24) and (25) are computed before the measurements are performed and they are valid for the employed geometry, discretizations and other parameters as long as the employed prior model and noise properties can be assumed to be feasible. Thus, these can be precomputed and the computational burden of the MAP estimates (15), (16), and (22) is essentially the same.

IV. Results

The Bayesian approach for the solution of the optical inverse problem of QPAT was tested with simulations. The noise statistics and the approximation errors were investigated. Furthermore, the three different MAP estimates were computed from simulated data sets utilizing the conventional and approximate noise models and approximation error modelling.

A. Geometry and Discretizations

A rectangular domain Ω of size 20 mm $\times$ 20 mm was considered. The Grüneisen coefficient was assumed to be a known constant with value $G = 1$. Four illuminations, one edge working as a light source in turn, were considered.

Two types of acoustic measurements were considered: fine and coarse sensor arrays. The fine sensor array was modelled using 316 ultrasound measurement positions evenly positioned around the target domain (80 detectors on each side of the domain). In the case of the coarse sensor array, 76 sensors (20 sensors on each side of the domain) were used.

1) Discretizations: For the forward and inverse acoustic computations, a larger computation domain of size 25 mm $\times$ 25 mm was created in order to minimize boundary effects. In all of the acoustic computations, the PML layer was located outside the computation domain. In the acoustic inverse problem, two discretizations were considered: a fine discretization consisting of 128 $\times$ 128 pixels and a coarse discretization with 64 $\times$ 64 pixels.

In the solution of the optical inverse problem, the domain Ω was discretized using 976 nodes and 1842 triangular elements for the FE-approximation of the DA. For the representation of the absorption and scattering, the domain Ω was discretized into $K = 1842$ disjoint elements Ω_k, and the absorption and scattering coefficients were represented in a piece-wise constant basis

$$\mu_a(r) \approx \sum_{k=1}^{K} \mu_{a_k}\chi_k(r) \tag{26}$$

$$\mu_s(r) \approx \sum_{k=1}^{K} \mu_{s_k}\chi_k(r) \tag{27}$$

TABLE I
Prior Mean η_x and Standard Deviations for the Background σ_x^{bg} and the Inclusions σ_x^{incl} Used in the Teaching and Reconstruction Prior Distributions

	Teaching		Reconstruction	
	$\mu_a(\mathrm{mm}^{-1})$	$\mu_s'(\mathrm{mm}^{-1})$	$\mu_a(\mathrm{mm}^{-1})$	$\mu_s'(\mathrm{mm}^{-1})$
η_x	0.01	1	0.01	1
σ_x^{bg}	0.001	0.1	0.002	0.2
σ_x^{incl}	0.002	0.2	0.01	1

where $\chi_k(r)$ is a characteristic function of the element Ω_k. Furthermore, the data for the inverse problem, the absorbed optical energy density, was represented using the same piece-wise constant basis.

2) Prior Model: In this work, the prior density $\pi(x)$ was utilized both in the solution of the MAP estimates (15), (16), and (22), in which case it worked as a regularizing penalty functional to alleviate the ill-posed nature of the problem, and when the noise model and the approximation error model were simulated. In both cases, the prior density was an informative smoothness prior [45], [48]. The informative smoothness prior is based on modifying a smoothing preprior into a Gaussian distribution. In this approach, quantitative information of the properties of the discretized parameter at some points, called marginalization points, is attached into the smoothing preprior. The information included is correlation length for the estimated parameters, which (roughly) is the prior estimate of the spatial size of the inhomogeneities in the target domain, prior mean, and a contrast for the background and the inhomogeneities. The correlation length used in the simulations for both absorption and scattering was 4 mm. Values for the mean and standard deviations of the teaching and reconstruction prior distributions for absorption and scattering are given in Table I. For more information about the informative smoothness prior, see e.g., [41], [45], [48].

B. Noise Models

The conventional noise model and the approximate noise model were generated for both the fine and the coarse acoustic sensor array setups.

1) Conventional Noise Model: For the conventional noise model, the noise was considered to be uncorrelated Gaussian distributed noise with zero mean. The standard deviation σ of the noise was set as 1% of the peak amplitude of the simulated data. Sample of the noise covariance structure is shown on the left image of Fig. 1.

2) Approximate Noise Model: To create the approximate noise model e, statistics of the noise was simulated by reconstructing noise samples using the time reversal method. To simulate the noise samples, first a set of time-varying pressure signals was simulated by solving the acoustic forward problem where the initial pressure was obtained by computing the FE-solution of the DA (1) together with the boundary condition (2) with optical parameters drawn from the informative smoothness prior and using equations (3) and (4). The mean and standard deviations of the teaching prior distributions are given in Table I. Then Gaussian distributed noise samples were generated with standard deviation of 1% of the peak amplitude

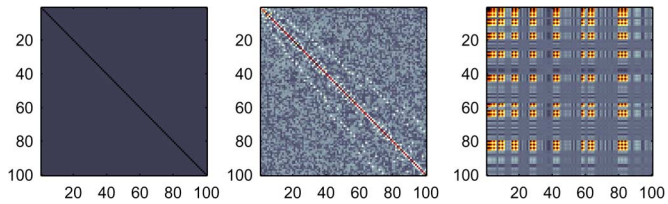

Fig. 1. Covariance structures (100 × 100 sample of a covariance matrix) of the conventional noise model Γ_σ (left image), the approximate noise model Γ_e (middle image) and the approximation error model Γ_ε (right image) in the fine discretization of the fine sensor array.

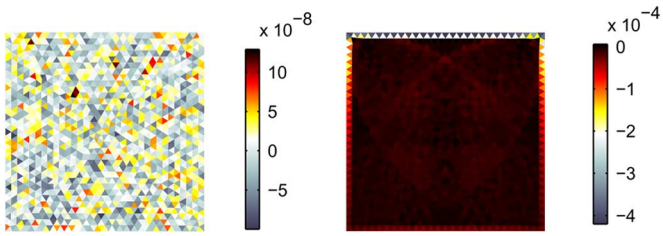

Fig. 2. Means of the approximate noise model e_* (left image) and the approximation error model ε_* (right image) when light is illuminated from the upper side of the domain in the fine discretization of the fine sensor array.

of the simulated time varying pressure signal. The number of simulated pressure signals used to define the peak amplitude was 80 and the number of noise samples generated for each of the pressure signals was 100. Both the fine (128 × 128 pixels) and the coarse (64 × 64 pixels) discretizations were considered. Note that the optical and acoustic forward solutions were utilized only to give a realistic amplitude for the noise and no other information of the forward solutions were included into the noise model. The mean and the covariance of the noise model e were approximated from reconstructed noise samples using (17) and (18).

The mean of the noise e_* with illumination from the upper side of the domain, simulated using the fine (128 × 128 pixels) acoustic discretization of the fine sensor array measurement setup, is shown in the left image of Fig. 2. A sample of the simulated noise covariance matrix Γ_e obtained using the fine discretization of the same setup is shown in the middle image of Fig. 1. As it can be seen, the mean of the noise does not show any structure and is close to zero. However, the covariance of the noise of the optical data is not uncorrelated. Thus, it can be expected that including information of the noise model, will improve the reconstructions.

C. Approximation Error Model

The approximation error mean and covariance were simulated for both the fine and the coarse sensor array setups as follows. First, 1200 samples $x^{(\ell)}$ were drawn from the teaching prior distribution given in Table I as in the case of the approximate noise model. The DA (1) together with the boundary condition (2) was solved using the FEM. Then samples of the absorbed optical energy density of the accurate model $A_\delta(x^{(\ell)})$ were calculated using (3).

The initial pressure was computed from these samples using (4) and the acoustic forward problem was solved using the k-space method with a 512 × 512 pixel discretization grid. Then, the acoustic inverse problem was solved using the time reversal method both in the fine (128 × 128 pixels) and the coarse (64 × 64 pixels) discretizations and samples of reduced model solutions $A_h(x^{(\ell)})$ were computed using (4) for both discretizations.

The samples of approximation error were computed from the samples of absorbed optical energy density of the accurate model $A_\delta(x^{(\ell)})$ and the reduced model $A_h(x^{(\ell)})$ using (23). Further, the mean and covariance of the approximation error were estimated using (24) and (25).

The mean of the approximation error ε_* when light is illuminated from the upper side of the domain simulated in the fine acoustic discretization of the fine sensor array measurement setup is shown in the right image of Fig. 2. Further, a sample of the simulated noise covariance matrix Γ_ε of the fine discretization of the same setup is shown in the right image of Fig. 1.

As it can be seen, the mean of the approximation error is nonzero close to the domain boundaries with the largest values close to the light source. Also the covariance has a structure different from the noise model covariances. These results show that the acoustic inversion affects the data. Furthermore, including this approximation error information in the optical inverse model is likely to improve the reconstructions.

D. Data Simulation

We simulated four datasets y using the following procedure. We considered absorption and scattering distributions shown on the top rows of Figs. 3 and 4. The anisotropy parameter was $g = 0.8$ throughout the domain. The absorption and scattering values were represented in the piecewise constant bases (26) and (27) using $K = 26166$ triangular elements.

First, the QPAT forward problem was solved. The DA (1) together with the boundary condition (2) was solved using the FEM. The FE-discretization consisted of 26166 triangular elements and 13284 nodes. The absorbed optical energy density distribution and the initial pressure were computed using (3) and (4), respectively. Then, the k-space method was used to simulate propagation of the pressure wave though the domain. The discretization of the computation domain consisted of 1024 × 1024 pixels. The time-varying acoustic pressure was recorded at 316 sensors located around the target corresponding to the fine sensor array setup and at 76 sensors corresponding to the coarse sensor array. Noise with a standard deviation of 1% of the peak amplitude of the simulated pressure signal was added to the both recorded datasets.

In order to obtain the data for the optical inverse problem, the acoustic inverse problem was solved using the time reversal method. The acoustic inverse problem was solved using both datasets in the fine (128 × 128 pixels) and coarse (64 × 64 pixels) discretizations. As a result, the initial pressure within the domain was obtained. The absorbed optical energy density in the reconstruction grid, which is the data y of the optical inverse problem, was computed from the initial pressure using (4) with Grüneisen coefficient $G = 1$.

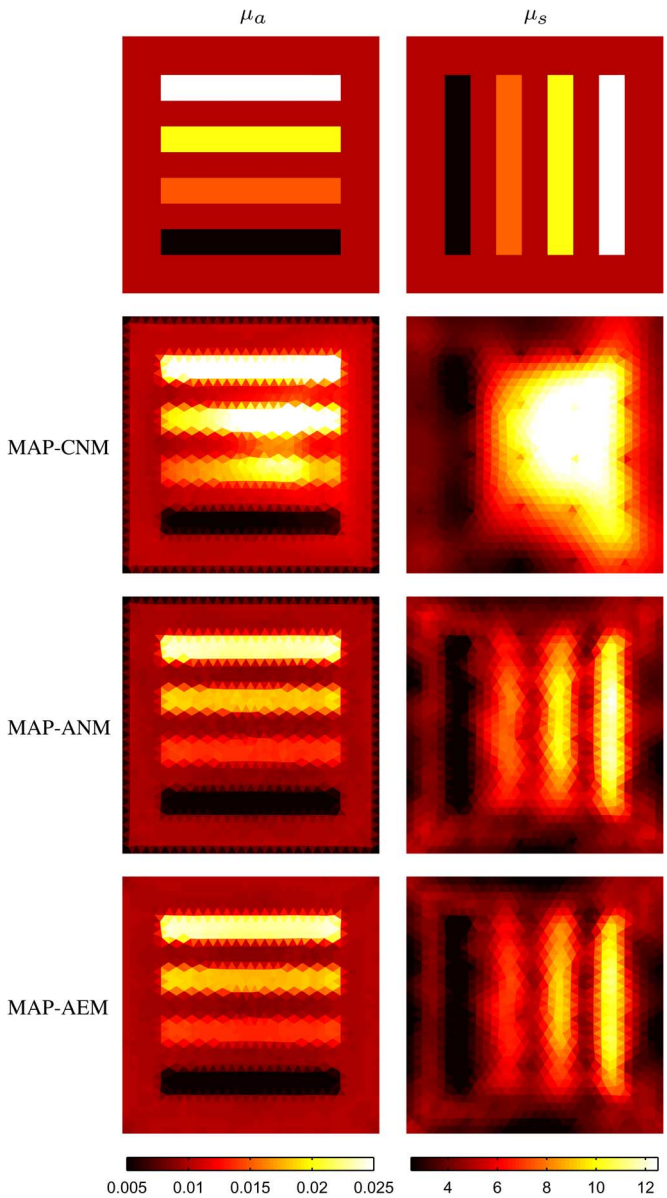

Fig. 3. Reconstructed absorption (left column) and scattering (right column) distributions. Images from top to bottom: simulated distributions (first row), reconstructions obtained with the noise models MAP-CNM (second row), MAP-ANM (third row), and error model MAP-AEM (fourth row) for the fine (128 × 128 pixels) acoustic discretization of the fine sensor array in 20 mm × 20 mm domain. The units of the colorbars are in mm^{-1}.

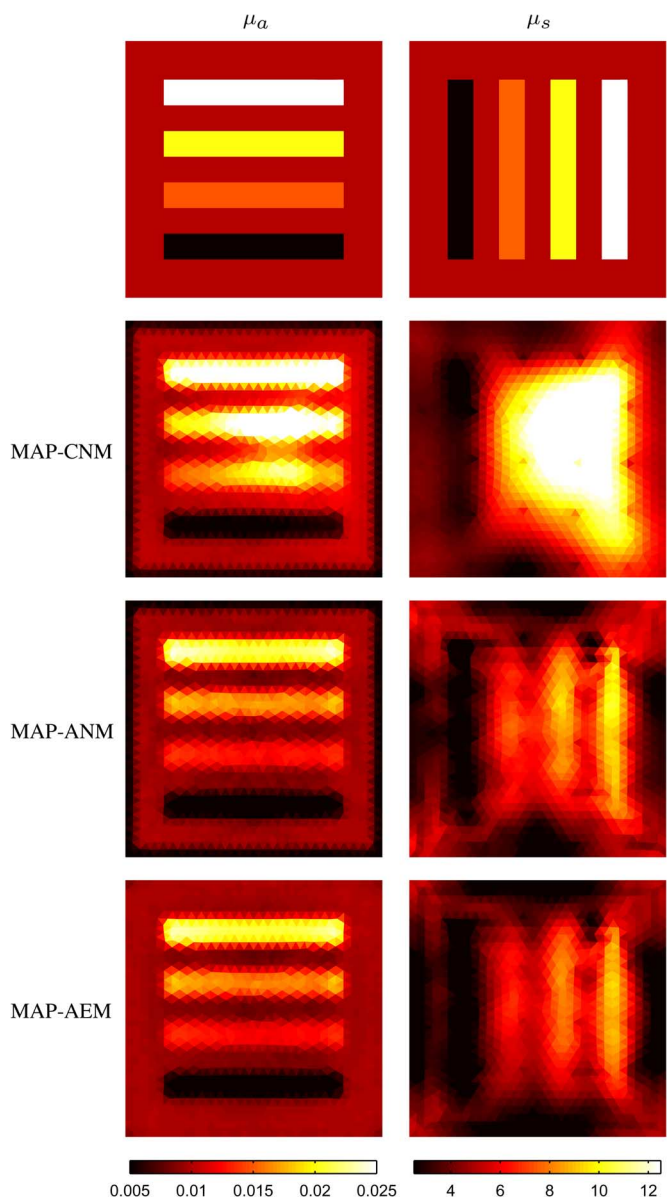

Fig. 4. Reconstructed absorption (left column) and scattering (right column) distributions. Images from top to bottom: simulated distributions (first row), reconstructions obtained with the noise models MAP-CNM (second row), MAP-ANM (third row), and error model MAP-AEM (fourth row) for the coarse (64 × 64 pixels) acoustic discretization of the fine sensor array in 20 mm × 20 mm domain. The units of the colorbars are in mm^{-1}.

E. Reconstructions

The MAP estimates of the three approaches were computed by minimizing (15) (MAP-CNM), (16) (MAP-ANM), and (22) (MAP-AEM) using a Gauss–Newton method equipped with a line search algorithm and positivity constraint. Data simulated using both fine and coarse acoustic discretizations of the fine and coarse sensor arrays and the corresponding noise and error models were considered. The prior distribution was the informative smoothness prior $\pi(x)$ described earlier with mean and standard deviations given in Table I.

Differences between the simulated and estimated absorption and scattering parameters were compared by computing the relative errors

$$E_{\mu_a} = 100\% \cdot \frac{\mu_a - \hat{\mu}_a}{\mu_a}, \quad E_{\mu_s} = 100\% \cdot \frac{\mu_s - \hat{\mu}_s}{\mu_s} \tag{28}$$

and the mean relative errors

$$\bar{E}_{\mu_a} = 100\% \cdot \frac{\|\mu_a - \hat{\mu}_a\|}{\|\mu_a\|}, \quad \bar{E}_{\mu_s} = 100\% \cdot \frac{\|\mu_s - \hat{\mu}_s\|}{\|\mu_s\|} \tag{29}$$

where μ_a and μ_s are the simulated absorption and scattering distributions interpolated to the solution space and $\hat{\mu}_a$ and $\hat{\mu}_s$ are the estimated values.

1) Reconstructions From Fine Sensor Array Data: The reconstructed absorption and scattering distributions from the data simulated using the fine acoustic discretization of the fine sensor array setup are shown in Fig. 3. The reconstructed absorption and scattering distributions from the data simulated using the coarse discretization of the same sensor array are shown in Fig. 4.

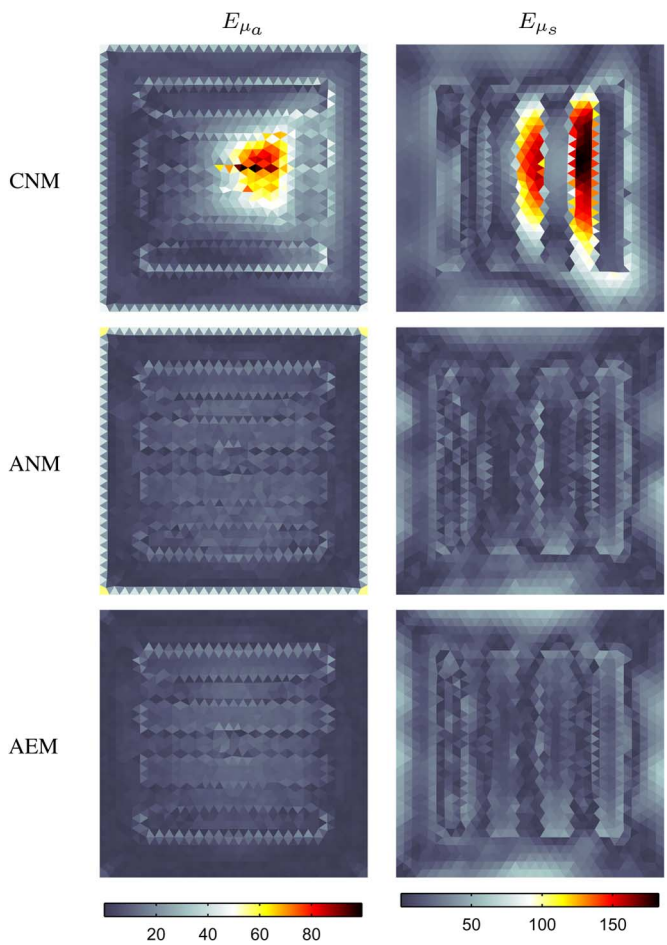

Fig. 5. Relative errors of absorption $E_{\mu_a}(\%)$ (left column) and scattering $E_{\mu_s}(\%)$ (right column) estimates obtained using the conventional noise model CNM (first row), approximate noise model ANM (second row), and approximation error modelling AEM (third row) in the fine (128 × 128 pixels) acoustic discretization of the fine sensor array.

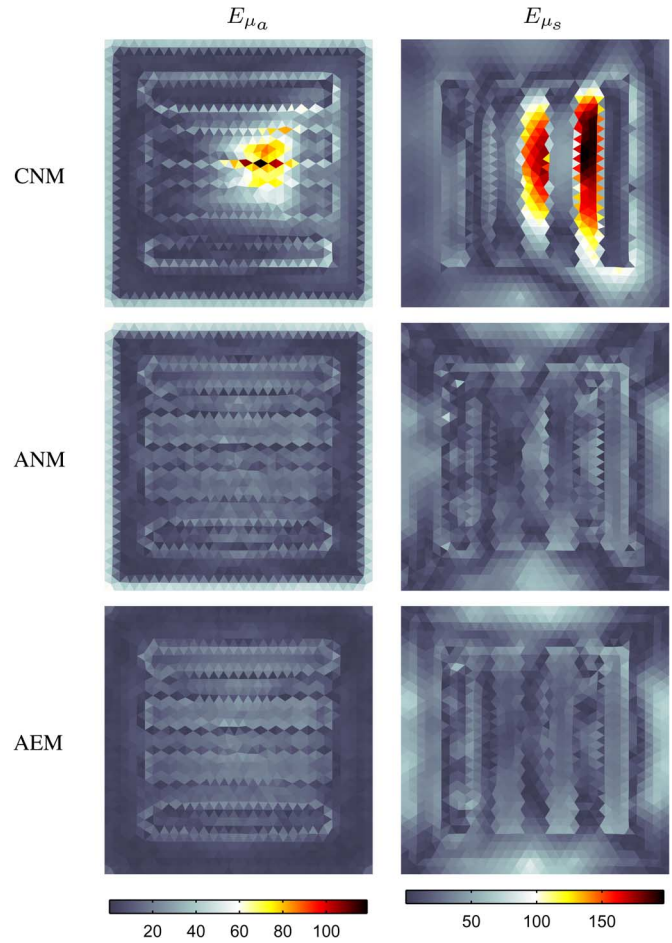

Fig. 6. Relative errors of absorption $E_{\mu_a}(\%)$ (left column) and scattering $E_{\mu_s}(\%)$ (right column) estimates obtained using the conventional noise model CNM (first row), approximate noise model ANM (second row), and approximation error modelling AEM (third row) in the coarse (64 × 64 pixels) acoustic discretization of the fine sensor array.

TABLE II
MEAN RELATIVE ERRORS OF ABSORPTION AND SCATTERING MAP ESTIMATES $\bar{E}_{\mu_a}$ AND $\bar{E}_{\mu_s}$, RESPECTIVELY, OBTAINED WITH NOISE MODELS MAP-CNM (15), MAP-ANM (16), AND ERROR MODEL MAP-AEM (22) FOR THE FINE (128 × 128 PIXELS) AND THE COARSE (64 × 64 PIXELS) ACOUSTIC DISCRETIZATIONS OF THE FINE SENSOR ARRAY

	128 × 128 pixels		64 × 64 pixels	
	$\bar{E}_{\mu_a}$ (%)	$\bar{E}_{\mu_s}$ (%)	$\bar{E}_{\mu_a}$ (%)	$\bar{E}_{\mu_s}$ (%)
MAP-CNM	25	43	25	48
MAP-ANM	12	19	19	27
MAP-AEM	8	23	15	33

The distributions of the relative errors for absorption and scattering are shown in Figs. 5 and 6. Furthermore, the mean relative errors are given in Table II.

2) Reconstructions From Coarse Sensor Array Data: The reconstructed absorption and scattering distributions from the data simulated using the fine acoustic discretization of the coarse sensor array setup are shown in Fig. 7. The reconstructed absorption and scattering distributions from the data simulated using the coarse discretization of the same sensor array are shown in Fig. 8.

Furthermore, the distributions of the relative errors for absorption and scattering are shown in Figs. 9 and 10 and the corresponding mean relative errors are given in Table III.

3) Discussion: As can be seen, the absorption and scattering estimates obtained with the conventional noise model (MAP-CNM) are not as good as the absorption and scattering estimates obtained with the approximate noise model (MAP-ANM) and approximation error model (MAP-AEM). In particular, the scattering inclusions are not distinguished when conventional noise model is applied. We believe that this is due to the minimization problem being more ill-posed when estimating scattering. This ill-posedness leads to inaccurate scattering estimates and therefore affects the accuracy of the absorption estimates as well. This difficulty in estimating absorption and scattering simultaneously due to low sensitivity of the likelihood to distinguish scattering was also noticed in [18] where it was shown that the scattering estimates can be improved by using data in logarithmic scale. Taking the logarithm is however an *ad hoc* method to scale the data basis and it does not have a theoretical explanation which noise modelling through the Bayesian approach offers.

Modelling of the noise improves both the absorption and scattering estimates significantly. The scattering inclusions

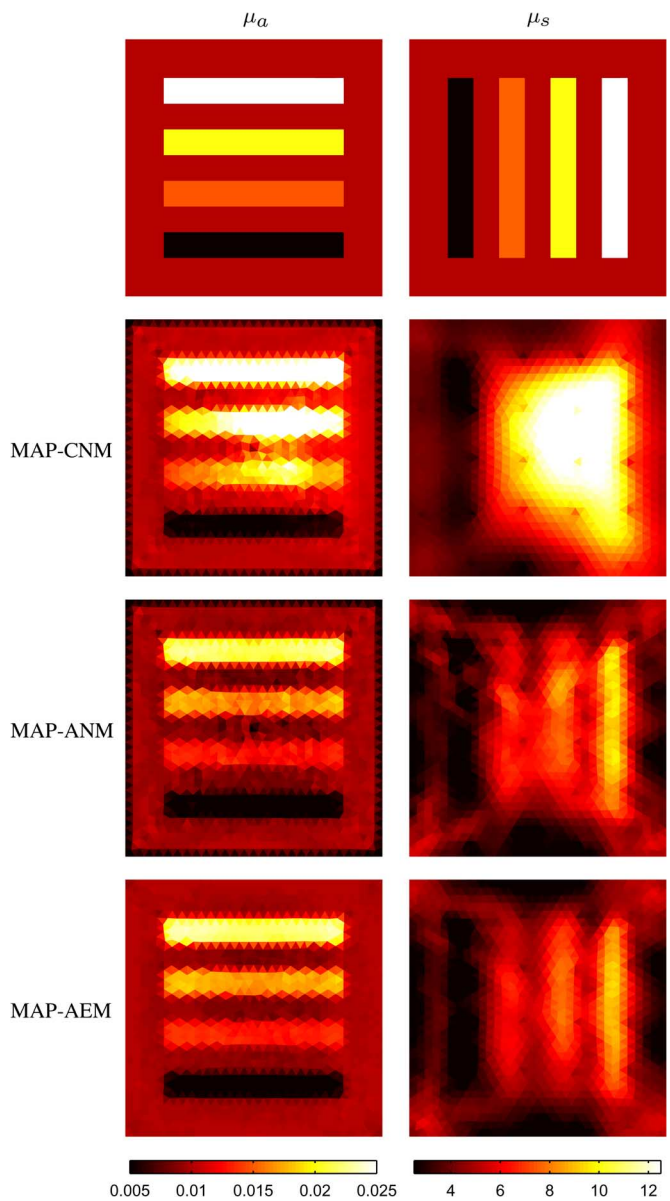

Fig. 7. Reconstructed absorption (left column) and scattering (right column) distributions. Images from top to bottom: simulated distributions (first row), reconstructions obtained with the noise models MAP-CNM (second row), MAP-ANM (third row), and error model MAP-AEM (fourth row) for the fine (128 × 128 pixels) acoustic discretization of the coarse sensor array in 20 mm × 20 mm domain. The units of the colorbars are in mm^{-1}.

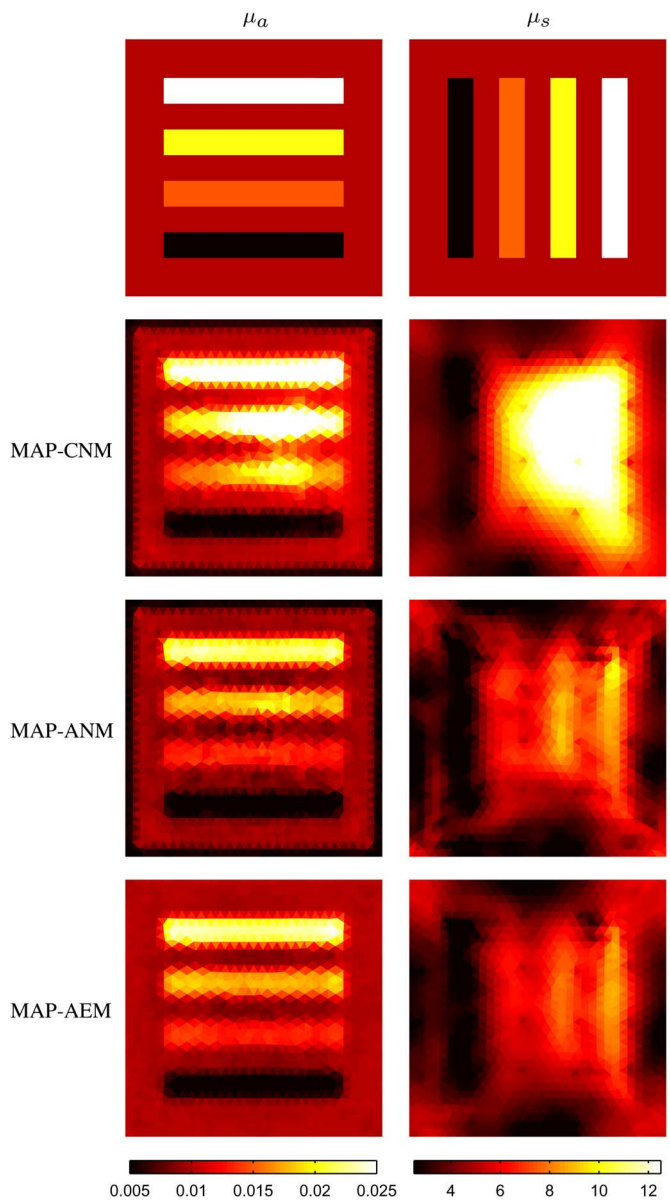

Fig. 8. Reconstructed absorption (left column) and scattering (right column) distributions. Images from top to bottom: simulated distributions (first row), reconstructions obtained with the noise models MAP-CNM (second row), MAP-ANM (third row), and error model MAP-AEM (fourth row) for the coarse (64 × 64 pixels) acoustic discretization of the coarse sensor array in 20 mm × 20 mm domain. The units of the colorbars are in mm^{-1}.

are distinguished well and the relative errors for absorption and scattering estimates are smaller when compared to the conventional noise model results. The absorption images show small errors close to the boundary which are likely to be due to data smoothing in the numerical implementation of the k-space method. Furthermore, when the coarse sensor array is applied, artefacts can be seen in the estimated absorption distributions inside and between the absorbing inclusions and everywhere in the scattering images.

The error close to boundaries in the absorption estimates is removed when the approximation error model is included in the reconstruction method. Also the other artefacts in the absorption images have reduced. The scattering estimates are of the same accuracy when compared to the approximate noise model results and significantly more accurate when compared to the conventional noise model case. It is also worth noticing that

TABLE III
MEAN RELATIVE ERRORS OF ABSORPTION AND SCATTERING MAP ESTIMATES $\bar{E}_{\mu_a}$ AND $\bar{E}_{\mu_s}$, RESPECTIVELY, OBTAINED WITH NOISE MODELS MAP-CNM (15), MAP-ANM (16) AND ERROR MODEL MAP-AEM (22) FOR THE FINE (128 × 128 PIXELS) AND THE COARSE (64 × 64 PIXELS) ACOUSTIC DISCRETIZATIONS OF THE COARSE SENSOR ARRAY

	128 × 128 pixels		64 × 64 pixels	
	$\bar{E}_{\mu_a}$ (%)	$\bar{E}_{\mu_s}$ (%)	$\bar{E}_{\mu_a}$ (%)	$\bar{E}_{\mu_s}$ (%)
MAP-CNM	24	43	25	46
MAP-ANM	17	29	18	32
MAP-AEM	11	30	11	31

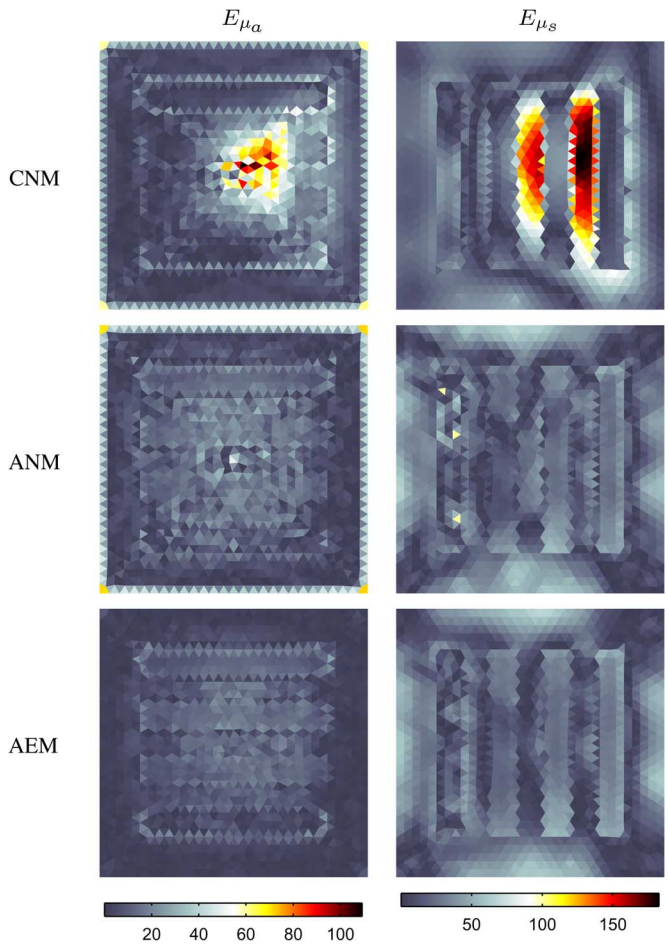

Fig. 9. Relative errors of absorption $E_{\mu_a}(\%)$ (left column) and scattering $E_{\mu_s}(\%)$ (right column) estimates obtained using the conventional noise model CNM (first row), approximate noise model ANM (second row), and approximation error modelling AEM (third row) in the fine (128×128 pixels) acoustic discretization of the coarse sensor array.

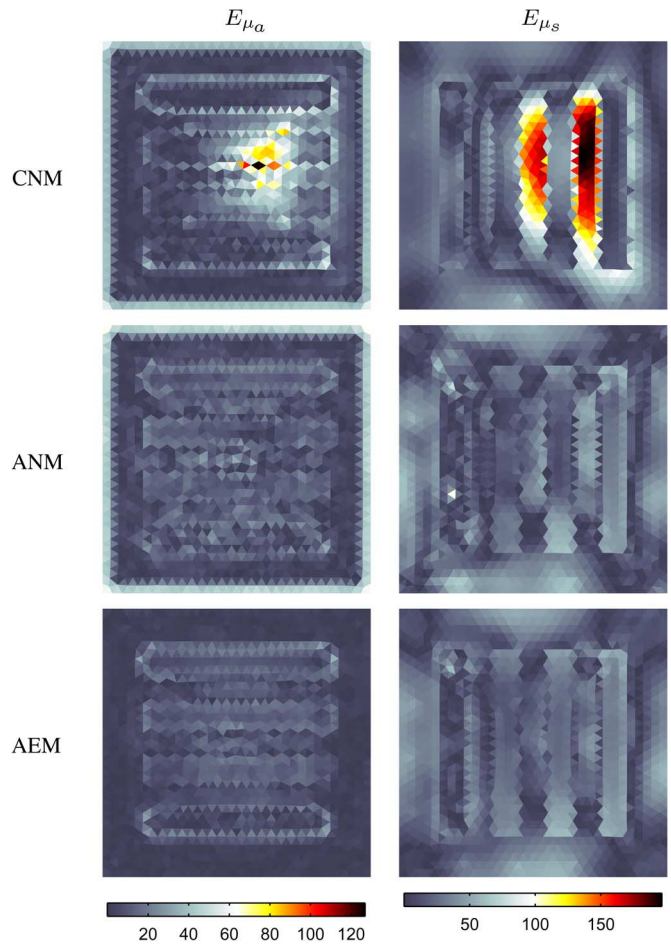

Fig. 10. Relative errors of absorption $E_{\mu_a}(\%)$ (left column) and scattering $E_{\mu_s}(\%)$ (right column) estimates obtained using the conventional noise model CNM (first row), approximate noise model ANM (second row), and approximation error modelling AEM (third row) in the coarse (64×64 pixels) acoustic discretization of the coarse sensor array.

the MAP-AEM estimates of absorption obtained using different acoustic sensor arrays and discretizations are approximately of the same magnitude. Thus, significant model reduction can be performed if the approximation error method is used.

V. Conclusion

In this paper, the optical inverse problem of QPAT in the framework of a Bayesian inversion was considered. In the optical reconstruction of QPAT, the data is obtained as a solution of an acoustic inverse initial value problem. Thus, both the data and the noise are affected by the acoustic solver. The noise of the optical data was modelled as Gaussian distributed with mean and covariance approximated by solving several acoustic inverse initial value problems using acoustic noise samples as data. Furthermore, the modelling errors of the acoustic solution method were considered using the Bayesian approximation error method. The developed noise model and the approximation error model were utilized in the optical inverse problem and the MAP estimates utilizing the conventional noise model, the approximate noise model and the approximation error modelling were computed. The results show that modelling of the noise and the approximation errors can improve the optical reconstructions of QPAT significantly by improving the accuracy of the estimated parameters and removing systematic artefacts caused by the acoustic solver. Furthermore, using the approximation error method enables the use of coarser discretizations and sensor arrays than the conventional approaches.

References

[1] M. Xu and L. V. Wang, "Photoacoustic imaging in biomedicine," *Rev. Sci. Instrum.*, vol. 77, p. 041101, 2006.
[2] C. Li and L. V. Wang, "Photoacoustic tomography and sensing in biomedicine," *Phys. Med. Biol.*, vol. 54, pp. R59–R97, 2009.
[3] , L. V. Wang, Ed., *Photoacoustic Imaging and Spectroscopy*. Boca Raton, FL: CRC Press, 2009.
[4] P. Beard, "Biomedical photoacoustic imaging," *Interface Focus*, vol. 1, pp. 602–631, 2011.
[5] B. Cox, J. G. Laufer, S. R. Arridge, and P. C. Beard, "Quantitative spectroscopic photoacoustic imgaging: A review," *J. Biomed. Opt.*, vol. 17, no. 6, p. 061202, 2012.
[6] P. Kuchment and L. Kunyansky, "Mathematics of thermoacoustic tomography," *Eur. J. Appl. Math.*, vol. 19, pp. 191–224, 2008.
[7] X. Jin and L. Wang, "Thermoacoustic tomography with correction for acoustic speed variations," *Phys. Med. Biol.*, vol. 51, pp. 6437–6448, 2006.
[8] Y. Hristova, P. Kuchment, and L. Nguyen, "Reconstruction and time reversal in thermoacoustic tomography in acoustically homogeneous and inhomogeneous media," *Inverse Problems*, vol. 24, p. 055006, 2008.

[9] C. Zhang and Y. Wang, "A reconstruction algorithm for thermoacoustic tomography with compensation for acoustic speed heterogeneity," *Phys. Med. Biol.*, vol. 53, pp. 4971–4982, 2008.

[10] R. Kowar and O. Scherzer, "Photoacoustic imaging taking into account attenuation," *Math. Algor. Tomogr.*, vol. 18, pp. 54–56, 2010.

[11] B. T. Cox and B. E. Treeby, "Artifact trapping during time reversal photoacoustic imaging for acoustically heteregeneous media," *IEEE Trans. Med. Imag.*, vol. 29, no. 2, pp. 387–396, Feb. 2010.

[12] B. E. Treeby, E. Z. Zhang, and B. T. Cox, "Photoacoustic tomography in absorbing acoustic media using time reversal," *Inverse Problems*, vol. 26, p. 115003, 2010.

[13] X. L. Deán-Ben, R. Ma, D. Razansky, and V. Ntziachristos, "Statistical approach for optoacoustic image reconstruction in the presence of strong acoustic heterogeneities," *IEEE Trans. Med. Imag.*, vol. 30, no. 2, pp. 401–408, Feb. 2011.

[14] R. W. Schoonover and M. A. Anastasio, "Compensation of shear waves in photoacoustic tomography with layered acoustic media," *J. Opt. Soc. Am. A*, vol. 28, no. 10, pp. 2091–2099, 2011.

[15] R. W. Schoonover, L. V. Wang, and M. A. Anastasio, "Numerical investigation of the effects of shear waves in transcranial photoacoustic tomography with a planar geometry," *J. Biomed. Opt.*, vol. 17, no. 6, p. 061215, 2012.

[16] C. Huang, L. Nie, R. W. Schoonover, L. V. Wang, and M. A. Anastasio, "Photoacoustic computed tomography correcting for heterogeneity and attenuation," *J. Biomed. Opt.*, vol. 17, no. 6, p. 061211, 2012.

[17] G. Bal and K. Ren, "Multi-source quantitative photoacoustic tomography in a diffusive regime," *Inverse Problems*, vol. 27, p. 075003, 2011.

[18] T. Tarvainen, B. T. Cox, J. P. Kaipio, and S. R. Arridge, "Reconstructing absorption and scattering distributions in quantitative photoacoustic tomography," *Inverse Problems*, vol. 28, p. 084009, 2012.

[19] A. Pulkkinen, V. Kolehmainen, J. P. Kaipio, B. T. Cox, S. R. Arridge, and T. Tarvainen, "Approximate marginalization of unknown scattering in quantitative photoacoustic tomography," *Inverse Problems Imag.*.

[20] B. T. Cox, S. R. Arridge, and P. C. Beard, "Estimating chromophore distributions from multiwavelength photoacoustic images," *J. Opt. Soc. Am. A*, vol. 26, no. 2, pp. 443–455, 2009.

[21] D. Razansky, J. Baeten, and V. Ntziachristos, "Sensitivity of molecular target detection by multispectral optoacoustic tomography (MSOT)," *Med. Phys.*, vol. 36, no. 3, pp. 939–945, 2009.

[22] J. Laufer, B. Cox, E. Zhang, and P. Beard, "Quantitative determination of chromophore concentrations form 2D photoacoustic images using a nonlinear model-based inversion scheme," *Appl. Opt.*, vol. 49, no. 8, pp. 1219–1233, 2010.

[23] G. Bal and K. Ren, "On multi-spectral quantitative photoacoustic tomography in a diffusive regime," *Inverse Problems*, vol. 28, p. 025010, 2012.

[24] D. Razansky, A. Buehler, and V. Ntziachristos, "Volumetric real-time multispectral optoacoustic tomography of biomarkers," *Nature Protocols*, vol. 6, no. 8, pp. 1121–1129, 2011.

[25] D. Razansky, "Multispectral optoacoustic tomography—Volumetric color hearing in real time," *IEEE Sel. Topics Quantum Electron.*, vol. 18, no. 3, pp. 1234–1243, May/Jun. 2012.

[26] J. Ripoll and V. Ntziachristos, "Quantitative point source photoacoustic inversion formulas for scattering and absorbing media," *Phys. Rev. E*, vol. 71, p. 031912, 2005.

[27] B. T. Cox, S. R. Arridge, K. P. Köstli, and P. C. Beard, "Two-dimensional quantitative photoacoustic image reconstruction of absorption distributions in scattering media by use of a simple iterative method," *Appl. Opt.*, vol. 45, pp. 1866–1875, 2006.

[28] B. Banerjee, S. Bagchi, R. M. Vasu, and D. Roy, "Quantitative photoacoustic tomography from boundary pressure measurements: Noniterative recovery of optical absorption coefficient from the reconstructed absorbed energy map," *J. Opt. Soc. Am A*, vol. 25, no. 9, pp. 2347–2356, 2008.

[29] T. Jetzfellner, D. Razansky, A. Rosenthal, R. Schulz, and K. H. Englmeier, "Performance of iterative optoacoustic tomography with experimental data," *Appl. Phys. Lett.*, vol. 95, p. 013703, 2009.

[30] L. Yao, Y. Sun, and H. Jiang, "Quantitative photoacoustic tomography based on the radiative transfer equation," *Opt. Lett.*, vol. 34, no. 12, pp. 1765–1767, 2009.

[31] H. Gao, H. Zhao, and S. Osher, Bregman methods in quantitative photoacoustic tomography UCLA, CAM Rep., 2010.

[32] L. Yao, Y. Sun, and H. Jiang, "Transport-based quantitative photoacoustic tomography: Simulations and experiments," *Phys. Med. Biol.*, vol. 55, pp. 1917–1934, 2010.

[33] R. J. Zemp, "Quantitative photoacoustic tomography with multiple optical sources," *Appl. Opt.*, vol. 49, no. 18, pp. 3566–3572, 2010.

[34] P. Shao, B. Cox, and R. Zemp, "Estimating optical absorption, scattering and Grueneisen distributions with multiple-illumination photoacoustic tomography," *Appl. Opt.*, vol. 50, no. 19, pp. 3145–3154, 2011.

[35] B. Cox, T. Tarvainen, and S. Arridge, , G. Bal, D. Finch, P. Kuchment, J. Schotland, P. Stefanov, and G. Uhlmann, Eds., "Multiple illumination quantitative photoacoustic tomography using transport and diffusion models," in *Tomography and Inverse Transport Theory (Contemporary Mathematics)*. Providence, RI: Am. Math. Soc., 2011, vol. 559, pp. 1–12.

[36] S. Bu, Z. Liu, T. Shiina, K. Kondo, M. Yamakawa, K. Fukutani, Y. Someda, and Y. Asao, "Model-based reconstruction integrated with fluence compensation for photoacoustic tomography," *IEEE Trans. Biomed. Eng.*, vol. 59, no. 5, pp. 1354–1363, May 2012.

[37] X. L. Deán-Ben, A. Buehler, V. Ntziachristos, and D. Razansky, "Accurate model-based reconstruction algorithm for three-dimensional optoacoustic tomography," *IEEE Trans. Med. Imag.*, vol. 31, no. 10, pp. 1922–1928, Oct. 2012.

[38] A. V. Mamonov and K. Ren, Quantitative photoacoustic imaging in radiative transport regime 2012, arXiv:1207.4664.

[39] X. Li and H. Jiang, "Impact of inhomogeneous optical scattering coefficient distribution on recovery of optical absorption coefficient maps using tomographic photoacoustic data," *Phys. Med. Biol.*, vol. 58, pp. 999–1011, 2013.

[40] T. Saratoon, T. Tarvainen, B. T. Cox, and S. R. Arridge, "A gradient-based method for quantitative photoacoustic tomography using the radiative transfer equation," *Inverse Problems*, vol. 29, p. 075006, 2013.

[41] J. Kaipio and E. Somersalo, *Statistical and Computational Inverse Problems*. New York: Springer, 2005.

[42] D. Calvetti and E. Somersalo, *Introduction to Bayesian Scientific Computing*. New York: Springer, 2007.

[43] J. Kaipio and E. Somersalo, "Statistical inverse problems: Discretization, model reduction and inverse crimes," *J. Comput. Appl. Math.*, vol. 198, pp. 493–504, 2007.

[44] J. Heino, E. Somersalo, and J. P. Kaipio, "Compensation for geometric mismodelling by anisotropies in optical tomography," *Opt. Exp.*, vol. 13, no. 1, pp. 296–308, 2005.

[45] S. R. Arridge, J. P. Kaipio, V. Kolehmainen, M. Schweiger, E. Somersalo, T. Tarvainen, and M. Vauhkonen, "Approximation errors and model reduction with an application in optical diffusion tomography," *Inverse Problems*, vol. 22, pp. 175–195, 2006.

[46] J. M. J. Huttunen and J. P. Kaipio, "Approximation errors in nonstationary inverse problems," *Inverse Problems Imag.*, vol. 1, no. 1, pp. 77–93, 2007.

[47] A. Lehikoinen, S. Finsterle, A. Voutilainen, L. M. Heikkinen, M. Vauhkonen, and J. P. Kaipio, "Approximation errors and truncation of computational domains with application to geophysical tomography," *Inverse Problems Imag.*, vol. 1, no. 2, pp. 371–389, 2007.

[48] V. Kolehmainen, M. Schweiger, I. Nissilä, T. Tarvainen, S. R. Arridge, and J. P. Kaipio, "Approximation errors and model reduction in three-dimensional diffuse optical tomography," *J. Opt. Soc. Am. A*, vol. 26, no. 10, pp. 2257–2268, 2009.

[49] A. Nissinen, L. M. Heikkinen, V. Kolehmainen, and J. P. Kaipio, "Compensation of errors due to discretization, domain truncation and unknown contact impedances in electrical impedance tomography," *Meas. Sci. Technol.*, vol. 20, p. 015504, 2009.

[50] T. Tarvainen, V. Kolehmainen, J. P. Kaipio, and S. R. Arridge, "Corrections to linear methods for diffuse optical tomography using approximation error modelling," *Biomed. Opt. Exp.*, vol. 1, no. 1, pp. 209–222, 2010.

[51] A. Nissinen, V. Kolehmainen, and J. P. Kaipio, "Compensation of modelling errors due to unknown domain boundary in electrical impedance tomography," *IEEE Trans. Med. Imag.*, vol. 30, no. 2, pp. 231–242, Feb. 2010.

[52] A. Lipponen, A. Seppänen, and J. Kaipio, "Nonstationary approximation error approach to imaging of three-dimensional pipe flow: Experimental evaluation," *Meas. Sci. Tech.*, vol. 22, p. 104013, 2011.

[53] J. Heiskala, V. Kolehmainen, T. Tarvainen, J. P. Kaipio, and S. R. Arridge, "Approximation error method can reduce artifacts due to scalp blood flow in optical brain activation imaging," *J. Biomed. Opt.*, vol. 17, no. 9, p. 096012, 2012.

[54] S. R. Arridge, "Optical tomography in medical imaging," *Inverse Problems*, vol. 15, pp. R41–R93, 1999.

[55] B. E. Treeby and B. T. Cox, "k-Wave: MATLAB toolbox for the simulation and reconstruction of photoacoustic wave fields," *J. Biomed. Opt.*, vol. 15, no. 2, p. 021314, 2010.

[56] B. T. Cox and P. C. Beard, "Fast calculation of pulsed photoacoustic fields in fluids using PHK-space methods," *J. Acoust. Soc. Am.*, vol. 117, no. 6, pp. 3616–3627, 2005.

[57] B. E. Treeby, T. K. Varslot, E. Z. Zhang, J. G. Laufer, and P. C. Beard, "Automatic sound speed selection in photoacoustic image reconstruction using an autofocus approach," *JBO Lett.*, vol. 16, no. 9, p. 090501, 2011.

[58] C. G. Constable, "Parameter estimation in non-Gaussian noise," *Geophys. J.*, vol. 94, pp. 131–142, 1988.

[59] J. A. Fessler, "Penalized weighted least-squares image reconstruction for positron emission tomography," *IEEE Trans. Med. Imag.*, vol. 13, no. 2, pp. 290–300, Jun. 1994.

[60] J. Qi, R. M. Leahy, S. R. Cherry, A. Chatziioannou, and T. H. Farquhar, "High-resolution 3D Bayesian image reconstruction using microPET small-animal scanner," *Phys. Med. Biol.*, vol. 43, pp. 1001–1013, 1998.

[61] J. Zhang, M. A. Anastasio, P. I. Rivière, and L. V. Wang, "Effects of different imaging models on least-squares image reconstruction accuracy in photoacoustic tomography," *IEEE Trans. Med. Imag.*, vol. 28, no. 11, pp. 1781–1790, Nov. 2009.

[62] M. Guven, L. Reilly-Raska, L. Zhou, and B. Yazıcı, "Discretization error analysis and adaptive meshing algorithms for fluorescence diffuse optical tomography: Part I," *IEEE Trans. Med. Imag.*, vol. 29, no. 2, pp. 217–229, Feb. 2010.

[63] M. Guven, L. Zhou, L. Reilly-Raska, and B. Yazıcı, "Discretization error analysis and adaptive meshing algorithms for fluorescence diffuse optical tomography: Part II," *IEEE Trans. Med. Imag.*, vol. 29, no. 2, pp. 230–245, Feb. 2010.

[64] L. Zhou and B. Yazıcı, "Discretization error analysis and adaptive meshing algorithms for fluorescence diffuse optical tomography in the presence of measurement noise," *IEEE Trans. Image Process.*, vol. 20, no. 4, pp. 1094–1111, Apr. 2011.